The Astrophysical Journal, 611:81–92, 2004 August 10

THEORETICAL Fe I–III EMISSION-LINE STRENGTHS FROM ACTIVE GALACTIC NUCLEI WITH BROAD-LINE REGIONS

T. A. A. Sigut
Department of Physics and Astronomy, The University of Western Ontario, London, ON N6A 3K7, Canada

and

Anil K. Pradhan and Sultana N. Nahar
Department of Astronomy, The Ohio State University, 174 West 18th Avenue, Columbus, OH 43210-1106
Received 2004 January 9; accepted 2004 April 20

ABSTRACT

We present theoretical iron emission line strengths for physical conditions typical of active galactic nuclei (AGNs) with broad-line regions. The non–local thermodynamic equilibrium (NLTE) models include a new and extensive treatment of radiative transfer in the Fe III ion, complementing the Fe II emission line strengths predicted in our earlier works. We also briefly present preliminary results for the Fe I emission from AGNs using a reduced atom model. We can satisfactorily reproduce the empirical UV Fe III emission line template of Vestergaard & Wilkes for the prototypical narrow-line Seyfert 1 galaxy I Zw 1, both in terms of the general Fe III flux distribution and the relative strength of the Fe III and Fe II emission. However, a number of detailed features are still not matched; the most prominent example is the strongest single Fe III feature observed in the I Zw 1 spectrum, UV47: it is predicted to be strong only in models suppressing Fe-H charge exchange reactions. We examine the role of variations in cloud turbulent velocity and iron abundance and carry out Monte Carlo simulations to demonstrate the effect of uncertainties in atomic data on the computed spectra.

Subject headings: atomic data — line: formation — line: identification — quasars: emission lines — supernovae: general

1. INTRODUCTION

The ultraviolet spectra of active galactic nuclei (AGNs) with broad-line regions (BLRs) exhibit a quasi-continuum of thousands of blended iron emission lines, dominated by Fe II (Wills et al. 1980a, 1980b); numerous Fe II transitions are also present in the optical (Boroson & Green 1992; Véron-Cetty et al. 2004) and near-infrared (Rudy et al. 2000, 2001; Rodríguez-Ardila et al. 2002). Since their recognition as a significant component of the BLR emission spectrum, these Fe II transitions have been the subject of intense observational scrutiny and theoretical modeling (Netzer 1980, 1990; Kwan & Krolik 1981; Netzer & Wills 1983; Wills et al. 1985; Elitzur & Netzer 1985; Collin-Souffrin et al. 1986, 1988; Penston 1987; Dumont & Collin-Souffrin 1990; Sigut & Pradhan 1998, 2003; Verner et al. 1999). Reproducing the strength of the Fe II emission has been a considerable challenge for traditional photoionized models of the BLR clouds; typically, the Fe II(UV + opt)/Hβ flux ratio is observed to be $\sim$10, ranging from $\sim$2 to near $\sim$30 in the case of superstrong Fe II emitters (Joly 1993; Graham et al. 1996).

However, Fe II is not the only component of the low-ionization emission spectrum of the BLR. Ultraviolet transitions of Fe III are also well established (Baldwin et al. 1996; Laor et al. 1997; Vestergaard & Wilkes 2001). Laor et al. (1997) identify a strong feature near 2418 Å in the spectrum of the prototypical narrow-line Seyfert 1 (NLS1) galaxy I Zw 1 as Fe III multiplet UV47. Most recently, Vestergaard & Wilkes (2001) provide a detailed analysis of the UV Fe III emission from I Zw 1 and use their observations to empirically derive Fe II *and* Fe III flux templates.

In our previous work (Sigut & Pradhan 2003, hereafter SP03), we constructed a detailed non-LTE radiative transfer model for Fe II, including 829 atomic levels, and predicted a large number ($\sim$23,000) of Fe II emission line strengths for conditions typical of the BLRs of AGNs. In this paper, we extend our earlier work on Fe II to detailed non-LTE models for Fe I–III. We compare these predictions to the observed UV I Zw 1 template.

2. ATOMIC DATA

The four lowest ionization stages of iron, Fe I–IV, were explicitly included in the calculations (although Fe IV was included as only a one-level atom). A summary of the complete iron model atom is given in Table 1. The final non-LTE atomic model includes 944 energy levels and 14,962 radiative bound-bound (rbb) transitions. With the exception of level energies, the majority of radiative and collisional atomic data were computed using methods developed under the Iron Project[1] (Hummer et al. 1993, hereafter IP.I). The ***R***-matrix method employed in the Iron Project (IP) ensures relatively uniform accuracy for the computed data. In the following sections, the IP atomic data will also be identified according to the number of the paper in the ongoing series published in *Astronomy & Astrophysics* (e.g., "IP.I" for the first paper in this series).

2.1. Fe I

A minimal Fe I atomic model was included in the calculation, mainly to predict the ionization fraction of Fe I in the various BLR models and provide preliminary flux estimates. While rare, Fe I fluxes have been tentatively identified in a few

[1] Complete references for the Iron Project are given at www.astronomy.ohio-state.edu/~pradhan.

TABLE 1
THE NON-LTE Fe I–IV MODEL ATOM

Atom	Number of NLTE Levels	Number of rbb Transitions
Fe I	77	185
Fe II	285	3892
Fe III	581	10885
Fe IV	1	0
Total	944	14962

Fe II-strong quasars (Boroson & Green 1992; Kwan et al. 1995). The Fe I atomic model consisted of 77 fine-structure levels (see Fig. 1) comprising 19 low-energy LS levels from the triplet, quintet, and septet spin symmetries. Energy levels and Einstein spontaneous transition probabilities (A_{ji}-values) for the 185 transitions were taken from the NIST compilation.[2] Photoionization cross sections were adopted from the ***R***-matrix calculations of Bautista & Pradhan (1997, hereafter IP.XX). Low-temperature, effective collision strengths for electron impact excitation of the first 10 metastable Fe I levels have been computed by Pelan & Berrington (1997, hereafter IP.XXI). All remaining collision strengths were estimated with the effective Gaunt factor approximation of van Regemorter (1962).

[2] See http://physics.nist.gov/PhysRefData/contents-atomic.html.

2.2. Fe II

Atomic data for Fe II have been extensively discussed by Sigut & Pradhan (1998, 2003). The IP data for collisions strengths for electron impact excitation were computed by Zhang & Pradhan (1995, hereafter IP.VI), for radiative transition probabilities, by Nahar (1995, hereafter IP.VII), and for photoionization cross sections, by Nahar & Pradhan (1994). We have adopted the smaller, 256 fine-structure level atom of Sigut & Pradhan (1998) for use in this calculation. The smaller number of Fe II levels allows a maximal number of Fe III energy levels to be simultaneously included. However, this smaller Fe II atom is still sufficiently large for realistic estimates of the flux and the inclusion of Lyα fluorescent excitation.

Among the atomic data for Fe II, we call particular attention to the $Fe^{2+} + H \Leftrightarrow Fe^{+} + H^{+}$ charge-exchange reaction rates of Neufeld & Dalgarno (1987). These large rates, computed in the Landau-Zener approximation, play an important role in the Fe II–Fe III ionization balance. However, their accuracy and efficacy in determining emission line strengths can be a source of uncertainly in the present calculations, as discussed later.

2.3. Fe III

Fe III was represented by 581 fine-structure energy levels (see Fig. 2), which include all Fe III levels with known energies

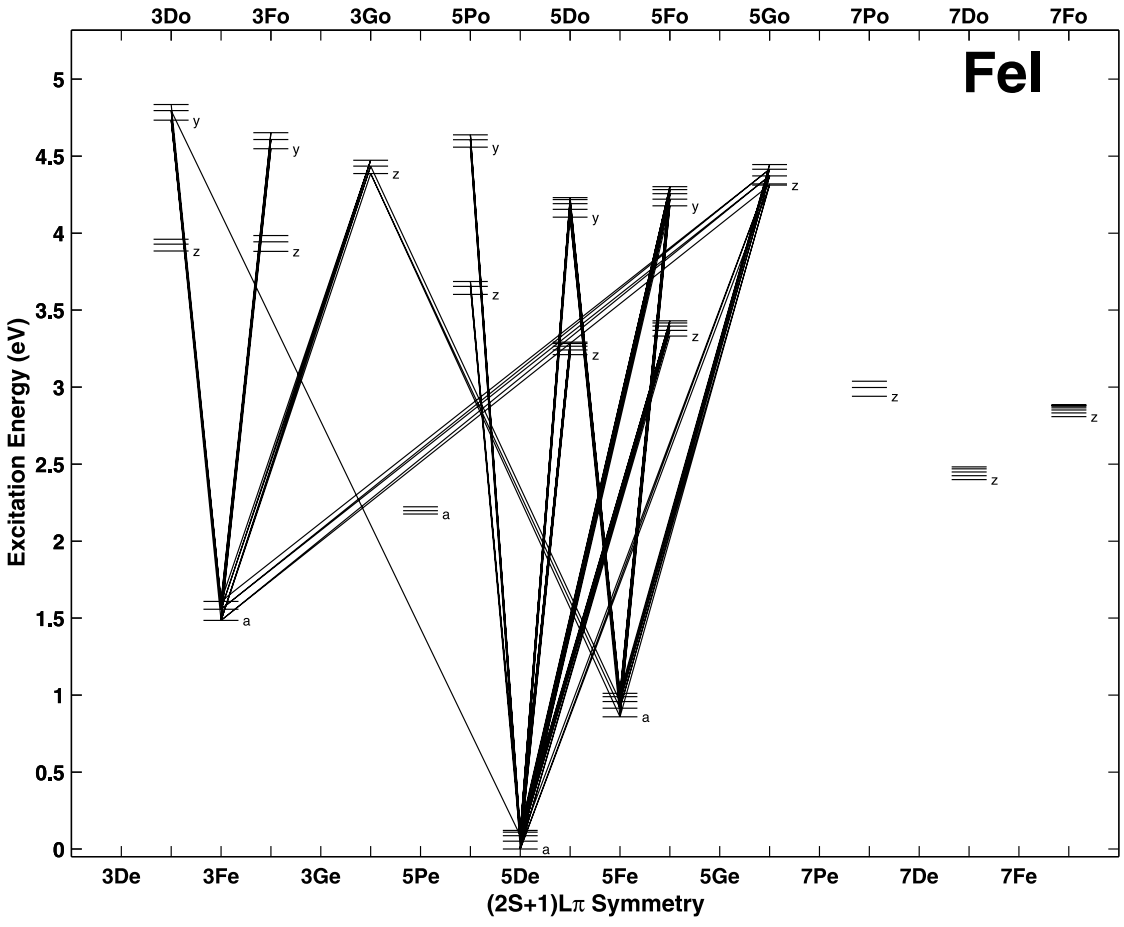

FIG. 1.—Grotrian diagram for Fe I showing all of the included energy levels and 116 ($f_{ij} > 10^{-3}$ and 2500 Å $\leq \lambda \leq$ 4500 Å) of the 285 included radiative transitions. The last included energy level, $y\ ^3D^o$, lies 3 eV below the Fe I ionization limit at 7.87 eV (*not shown*).

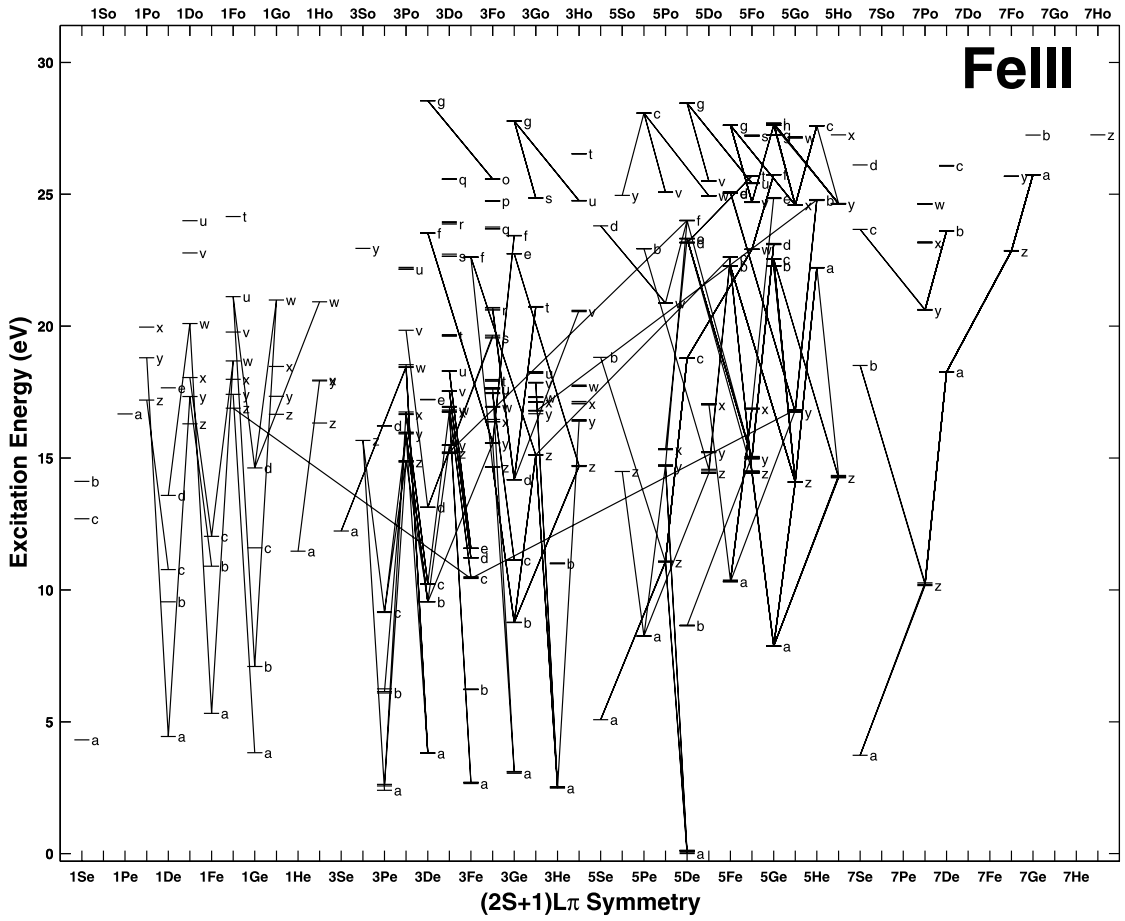

FIG. 2.—Grotrian diagram for Fe III showing all of the included energy levels and the 286 radiative transitions with $f_{ij} > 0.2$ and $\lambda < 5000$ Å. as predicted by Kurucz (1992). These transitions are only a tiny fraction of the total number of radiative transitions included in the calculation. The last energy level included, $g\ ^3D^e$, lies 2.1 eV below the Fe III ionization limit at 30.65 eV (*not shown*).

(see the NIST compilation; also Nahar & Pradhan 1996) We have used four principal sources to compile the required A_{ji}-values for Fe III transitions: the NIST critically evaluated database; the ***R***-matrix results of Nahar & Pradhan (1996, hereafter IP.XVII) for dipole-allowed ($\Delta S = 0$) transitions[3]; the Hartree-Fock calculations of Ekberg (1993), which also treats intersystem ($\Delta S \neq 0$) transitions; and the extensive semiempirical calculations of Kurucz (1992).

Photoionization cross sections were adopted from Nahar & Pradhan (IP.XVII). Collision strengths for electron impact excitation were adopted from Zhang (1996, hereafter IP.XVIII). All remaining collision strengths were estimated with the Gaunt factor approximation. Charge exchange reactions with Fe IV were also included following Kingdon & Ferland (1996).

3. CALCULATIONS

The iron line fluxes were calculated using the procedure of SP03. Briefly, a background temperature and density structure for a single BLR cloud of a given ionization parameter and total particle density was computed with CLOUDY (Ferland, 1991). The shape of the photoionizing continuum was taken to be that of Mathews & Ferland (1987). Given this fixed, one-dimensional model, the coupled equations of radiative transfer and statistical equilibrium were solved for a self-consistent set of iron level populations and line fluxes. A complete discussion of the system of equations solved, including the treatment of fluorescent excitation by Lyα and Lyβ, and the implementation details, are given in SP03. We note that our treatment of fluorescent excitation involves first the construction of the full frequency-dependent, PRD (partial-redistribution) source functions for Lyα and Lyβ, and then their inclusion in the total monochromatic source functions used in the radiative transfer solutions for all overlapping iron rbb transitions. All of the iron radiative transitions assumed complete redistribution over a Doppler line profile with a width given by

$$\Delta\nu_{\rm D} = \sqrt{\frac{2kT}{m_{\rm Fe}} + v_t^2}. \quad (1)$$

Here $m_{\rm Fe}$ is the mass of an iron atom and v_t is the internal turbulent velocity of the cloud.[4]

In the current work, each set of iron fluxes is specified by four model parameters representing the BLR cloud: the ionization parameter, the total particle density, the (internal) cloud

[3] Identification of the calculated (bound) Fe III levels and their correspondence with the experimental NIST energy levels was performed by Nahar & Pradhan (1996) via the ELEVID code of Nahar (1995).

[4] Turbulent velocity is used to refer to what is commonly denoted *microturbulence* by stellar astronomers; this velocity represents the width of a Gaussian distribution of turbulent motions small in scale compared to unit optical depth. These motions act to broaden the line profile (eq. [1]), and thus can alter the radiative transfer solution in each line.

TABLE 2
THE SINGLE-ZONE BLR MODELS

Label	U_{ion}	n_H (cm^{-3})	N_H (cm^{-3})
u13h96	$10^{-1.3}$	$10^{9.6}$	10^{23}
u13h11	$10^{-1.3}$	$10^{11.6}$	10^{23}
u20h96	10^{-2}	$10^{9.6}$	10^{23}
u20h11	10^{-2}	$10^{11.6}$	10^{23}
u30h96	10^{-3}	$10^{9.6}$	10^{23}
u30h11	10^{-3}	$10^{11.6}$	10^{23}

turbulent velocity, and the iron abundance relative to hydrogen. Table 2 identifies the different BLR models constructed in this work and the associated ionization parameters, particle densities, and total column densities.

4. IRON IONIZATION BALANCE

The ionization balance among the four lowest ionization stages of iron was self-consistently calculated simultaneously with the level populations. Expression for the total and level-specific photo and collisional ionization-recombination rates are given in SP03. A small correction was applied at each depth for the fraction of iron more highly ionized than Fe IV, with this correction being estimated by CLOUDY.

Our self-consistent procedure is different from Verner et al. (1999), who first solve for the iron ionization balance in isolation, balancing photoionization from the ground states against effective recombination rates, and then solve for the individual (Fe II) level populations using a fixed ionization structure. While this approximation is typical of nebular work where the population in the excited states is very small, densities in the BLR may approach $\sim 10^{+9}$–10^{+11} particles per cm^3, high enough to warrant a detailed treatment of photoionization from excited states in the calculation of the ionization balance. Another advantage of our approach is that no a priori assumptions are made as to the optical depths in the radiative transitions forming the recombination cascade (assumptions usually expressed as "Case A" or "Case" B, following Osterbrock 1989, for example); a self-consistent solution is automatically obtained.

Figure 3 shows the Fe I–Fe IV ionization balance for all the models of Table 2 assuming a solar iron abundance and a turbulent velocity of 10 km s^{-1} (at 10^4 K, the thermal widths of the iron lines are $\sim$2 km s^{-1}). At large optical depths in the Lyman continuum, Fe II is *always* the dominant iron species. However, closer to the illuminated face, the ionization parameter plays a strong role; for the lowest ionization parameter considered, Fe III dominates in the outer layers, while at the higher ionization parameters, Fe IV is the dominant species, with Fe III confined to a narrow zone at intermediate Lyman continuum optical depths. Also shown in Figure 3 is the hydrogen ionization balance as predicted by CLOUDY. The ionization of hydrogen has a strong influence on the iron ionization balance not only through the obvious effect of its

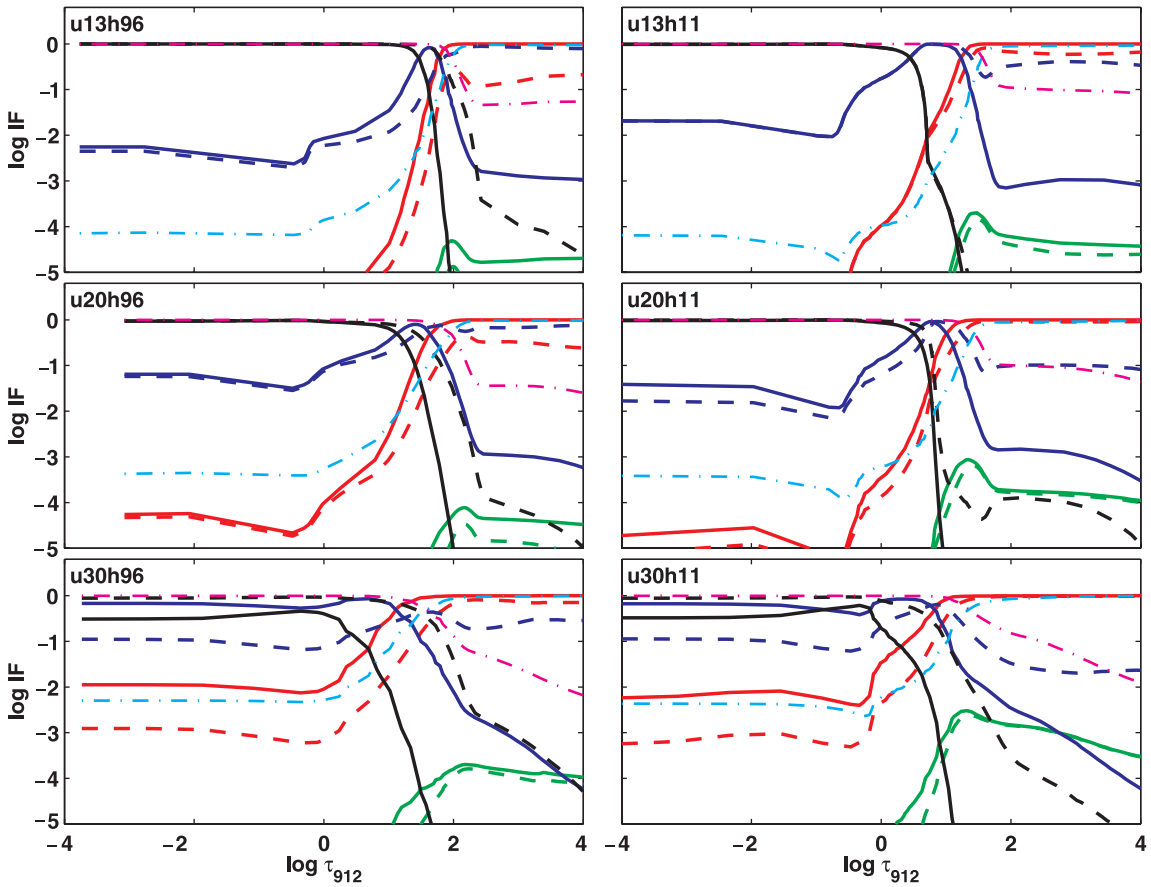

FIG. 3.—Predicted Fe I–Fe IV ionization balances for all of the BLR models of Table 2 assuming the solar iron abundance and an internal turbulent velocity of 10 km s^{-1}. The sold lines are calculations including Fe-H charge-exchange reactions, and the dotted lines are calculations without such charge-exchange reactions. The iron ions can be identified by the line colors: Fe I (*green lines*), Fe II (*red lines*), Fe III (*blue lines*), and Fe IV (*black lines*). Also shown in each panel is the hydrogen ionization balance decomposed into H I (*magenta dash-dotted line*) and H II (*pink dash-dotted line*).

TABLE 3
IRON FLUXES FOR THE BLR MODELS

Model (1)	F_{tot} (2)	% Fe I (3)	% Fe II (4)	% Fe III (5)
Solar Abundance, $V_t = 10$ km s^{-1}				
u30h96	2.246E+05	0.3	96.3	3.4
u30h11	5.393E+06	2.9	88.8	8.3
u20h96	1.479E+06	0.2	94.5	5.4
u20h11	2.470E+07	3.3	81.9	14.8
u13h96	4.698E+06	0.2	94.1	5.7
u13h11	1.572E+08	1.2	63.1	35.7
Solar Abundance, $V_t = 50$ km s^{-1}				
u30h96	2.936E+05	0.3	95.9	3.9
u30h11	1.006E+07	2.1	92.9	5.0
u20h96	2.366E+06	0.1	94.8	5.1
u20h11	6.687E+07	1.5	89.1	9.4
u13h96	8.840E+06	0.1	95.2	4.7
u13h11	4.198E+08	0.5	74.3	25.2
3× Solar Abundance, $V_t = 10$ km s^{-1}				
u30h96	5.958E+05	0.3	96.7	3.0
u30h11	1.186E+07	2.9	87.0	10.0
u20h96	3.471E+06	0.2	94.6	5.2
u20h11	4.004E+07	4.8	76.8	18.4
u13h96	1.003E+07	0.3	93.9	5.9
u13h11	2.520E+08	1.9	55.1	43.0

NOTES.—The total flux, F_{tot} in ergs cm^{-2} s^{-1}, is for 1500 Å $\leq \lambda \leq$ 5000 Å. Cols. (3)–(5) give the percentage contribution of each iron ion to the total flux. The models are identified as in Table 2.

opacity on the local ionizing radiation field, but also through strong charge-exchange reactions, $Fe^{2+} + H \Leftrightarrow Fe^{+} + H^{+}$.

Figure 3 also shows the predicted ionization fractions in the same set of BLR models except neglecting Fe-H charge-transfer reactions. There are significant differences, most notably for the higher ionization parameters at the lower particle density considered, models u20h96 and u13h96. The absence of charge exchange reactions in these models leads to Fe III, and not Fe II, as the dominant iron ionization stage throughout the cloud model. The influence of the charge-exchange reactions on the predicted iron fluxes will be discussed in a later section; such models *may* be partially supported by observation of I Zw 1 as they are better able to account for an intense feature near 2418 Å identified by Laor et al. (1997) as Fe III UV47. We note that the charge exchange ionization and recombination rates for $Fe^{2+} + H \Leftrightarrow Fe^{+} + H^{+}$ predicted by Neufeld & Dalgarno (1987) were obtained in the rather crude Landau-Zener approximation (see Flower 1990; also Kingdon & Ferland 1996), and it is not inconceivable that this rate may be significantly overestimated.

Finally, we note that the predicted fraction of Fe I in all cases, including the lowest ionization parameter considered, is very small, $\ll 10^{-3}$. The question of whether such a small neutral fraction can account for the tentatively identified Fe I features in AGN spectra will be addressed in a later section.

5. PREDICTED Fe III FLUXES

Table 3 gives the total iron fluxes in the wavelength interval of 1500–5000 Å for the single-zone BLR cloud models of Table 2. The effect of increasing the cloud turbulent velocity from 10 to 50 km s^{-1} and of tripling the iron abundance relative to hydrogen are also given. The total flux is broken down into the percentage contributions of each of the iron ions. The higher density models with the larger ionization parameters, models u20h11 and u13h11, predict the largest contribution of the flux arising from Fe III, approaching ~35% in model u13h11. As also seen from the table, the percentage contribution of Fe III tends to decrease with increasing turbulent velocity (except for model u30h96) and increases with an enhanced iron abundance; the u13h11 model, with a threefold enhancement of the iron abundance, comes close to having an equal flux split between Fe II and Fe III. It should be borne in mind that these comparisons are with the significantly smaller atom Fe II of Sigut & Pradhan (1998) to allow the simultaneous treatment of the a large Fe III atom.

Figures 4 and 5 show the wavelength distributions of the emitted iron line fluxes for the u20h96 and u13h11 models, respectively, in the case of a solar iron abundance and 10 km s^{-1} of turbulent velocity. The lower wavelength limit has been extended down from the 1500 Å of Table 3 to 500 Å in order to show the complete Fe III spectrum. The separate panels in these plots show the total line flux as well as the contributions from the individual iron ions. There is a striking difference in the Fe III fluxes predicted for these two models. For u20h96, the strongest Fe III emission occurs at wavelengths near 1900 Å. These transitions represent decays from the lowest odd-parity Fe III level, $z\ ^7P^o$, to $a\ ^7S^e$ and are the only possible $\Delta S = 0$ transitions (see Fig. 2). Intersystem ($\Delta S \neq 0$) transitions from $z\ ^7P^o$ to $a\ ^5D^e$, the Fe III ground state, giving lines near 1220 Å, and to $a\ ^5S^e$, giving lines near 2400 Å (multiplet UV47), are also present but weak. The multiplet UV47 transitions identified as the strongest Fe III features in the spectrum of I Zw 1 by

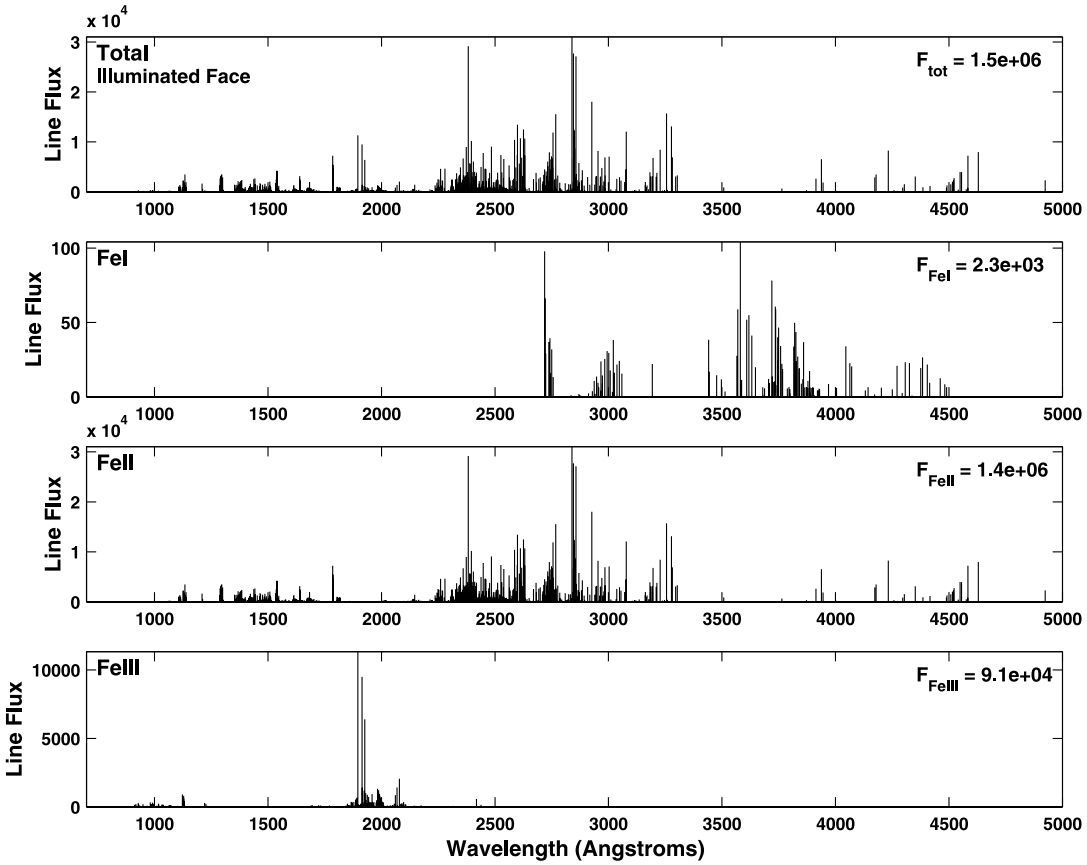

FIG. 4.—Predicted iron emission-line spectrum from the illuminated cloud face of BLR model u20h96. Each iron emission line is represented by a spike at its wavelength with a height equal to the total integrated line flux in ergs cm^{-2} s^{-1}. The top panel gives the total Fe I–Fe III line flux, while the lower panels show the contributions of the individually identified iron ions. The flux summed over all lines in each panel is also given.

Laor et al. (1997) will be further discussed in § 8.1. Decays from the only other low-lying odd-parity level, $z\ ^5P^o$, about 0.8 eV above $z\ ^7P^o$, are not prominent in the predicted spectrum for u20h96. A number of $\Delta S = 0$ decay paths from this level are possible, including decays to the Fe III ground state, $a\ ^5D^e$, which result in transitions near 1120 Å, and decays to $a\ ^5P^e$ and $b\ ^5D^e$, which give rise to transitions with $\lambda > 4000$ Å.

The higher ionization parameter, higher density model u13h11 presents a radically different picture. Now, in addition to the Fe III transitions around 1900 Å discussed above, Fe III emission lines fill the region around 1000 Å and dominate the total Fe III emission. The 1000 Å region is filled with decays from the numerous odd-parity levels near ~15 eV to the lowest even parity levels (<5 eV) of each spin system. The spectral region around 2000 Å is now filled with strong Fe III emission arising principally from the decay of odd parity levels to the numerous even parity levels near ~10 eV. As noted in Table 3, a significant fraction of the total iron flux comes out in the form of Fe III transitions.

In both of these models, fluorescent excitation by Lyα is unimportant due to the absence of significant line-overlap with any Fe III transitions. However, fluorescent excitation by Lyβ offers more potential. There are transitions from several low-lying, even-parity triplet states within a few Ångstroms of Lyβ (at 1025.72 Å): $a\ ^3P^e$–$z\ ^5S^o$ at 1025.71 Å ($f_{ij} = 0.0022$), $a\ ^3D^e$–y $^3P^o$ at 1024.11 Å ($f_{ij} = 0.023$), and $a\ ^3D^e$–y $^3P^o$ at 1026.79, 1026.88 Å ($f_{ij} = 0.026, f_{ij} = 0.0011$). Reperforming the u20h96 model without Lyβ fluorescent excitation resulted in a reduction in the total predicted Fe III flux of only about 12%; the reduction in the case of u13h11 from the absence of Lyβ fluorescent excitation was negligible.

6. PREDICTED Fe I FLUXES

According to Table 3, ~0.1%–5% of the total iron line flux comes out in transitions of Fe I. In Figure 5, representing model u13h11, the predicted emission due to Fe I in the 2700–4500 Å region is, although quite weak, not entirely negligible. This is illustrated in the second panel from the top in Figure 5; the strongest transitions present in this figure are just those expected from the Fe I Grotrian diagram of Figure 1, namely decays from low-lying odd parity levels between ~3.5 to 4.5 eV to the three lowest even parity states, the $a\ ^5D^e$ ground state, $a\ ^5F^e$, and $a\ ^3F^e$. The strongest predicted multiplet is 23, $z\ ^5g^o$–$a\ ^5F^e$, giving lines near 3600 Å. Such multiplets of Fe I have been tentatively identified in PHL 1092 by Bergeron & Knuth (1980) and Kwan et al. (1995) and in IRAS 07598+6508 by Kwan et al. Both objects are Fe II-strong quasars. The current calculations tend to support these identifications and the occurrence of Fe I transitions in some AGN spectra. Comparing our predictions to the IRAS 07598+6508 spectrum given by Kwan et al. (their Fig. 1),[5] we note that the observed Fe I flux relative to the nearby Fe II flux between 3600–3800 Å is much larger than predicted by our models, even when considering the effect of the tentative Ti I blends identified by

[5] Note that Kwan et al. use the observed wavelength scale, which is redshifted from Fig. 5 by $z = 0.1483$.

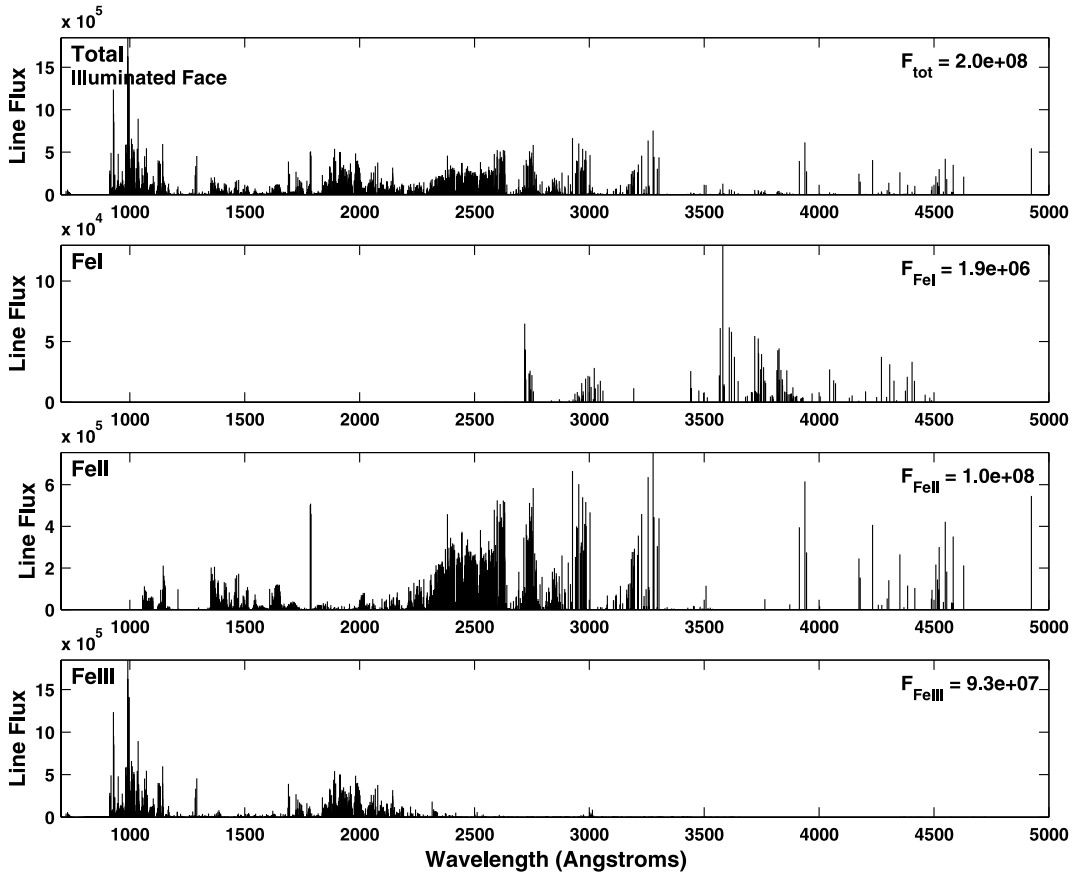

FIG. 5.—Same as Fig. 4, but for BLR model u13h11.

Kwan et al. However, it is likely that our models underestimate the Fe I flux; the very limited Fe I atomic model employed artificially suppresses recombination by omitting energy levels within ~3 eV of the continuum (see Carlsson et al. 1992 or Sigut & Lester 1996 for a discussion of this effect). This acts both to reduce the recombination contribution the line fluxes and to lower the Fe I ionization fraction, which also leads to weaker lines. We plan to extend our treatment of the Fe I atomic model in the future to provide more realistic flux estimates to compare with these observations.

7. DEPENDENCE OF IRON FLUX ON BLR CLOUD PARAMETERS

Figure 6 summarizes the dependence of the Fe I, Fe II, and Fe III fluxes on the various model parameters. The trend of increasing iron line fluxes with both ionization parameter and particle density is evident, as well as the maximization of the Fe III fluxes for the higher ionization parameter models. When viewing this figure, it should be remembered that the underlying BLR cloud model is kept fixed; the predicted Fe II–III net cooling has not been input into CLOUDY to recompute the BLR cloud model. This latter step could be important as the net iron line cooling may have a strong thermostatic effect on the BLR cloud structure.

Figure 6 also shows increased flux in Fe II and Fe III for either an increased cloud turbulent velocity or an increased iron abundance. Interestingly, however, the predicted Fe I flux does not depend on the internal cloud turbulent velocity. The lines of Fe I are weak and unsaturated so are insensitive to the turbulent velocity, contrary to the lines of the other ionization stages. From this figure it might seem possible that the internal cloud turbulent velocity could be deduced from the spectrum of an object exhibiting lines of both Fe I and Fe II. In fact, this is the classic technique in stellar atmospheres to determine the turbulent velocity dispersion (often dubbed microturbulence)—forcing weak and strong lines to be reproduced in strength by the same abundance. It might be worthwhile to attempt this in AGNs; however, the situation is much more complex as the entire BLR spectrum is likely not formed within a single cloud or ensemble of identical clouds (Baldwin et al. 1995); the question would arise as to whether clouds of different ionization parameters and particle densities would have similar turbulent velocities. Nevertheless, it would be still worthwhile to attempt this investigation. Knowledge of the intrinsic width of an emission line for individual clouds in the BLR has important implications on the uncertain nature of the BLR clouds themselves. Narrow, near thermal widths of ~10 km s^{-1} imply large numbers of BLR clouds in order to reproduce the smooth observed line profiles (Arav et al. 1997). Much larger intrinsic widths would require fewer clouds to produce smooth profiles, perhaps allowing stellar models for the BLR clouds to become viable (Peterson et al. 1999).

8. COMPARISON TO I Zw 1 Fe II–III UV TEMPLATE

Vestergaard & Wilkes (2001) provide an empirical Fe II–Fe III UV template (1250 Å $\leq \lambda \leq$ 3080 Å) derived from I Zw 1, the prototypical narrow-line Seyfert 1 galaxy. One of the main results of this work is the careful documentation of extensive Fe III emission from I Zw 1, building on the identifications of Laor et al. (1997). Figure 7 compares four of our basic models

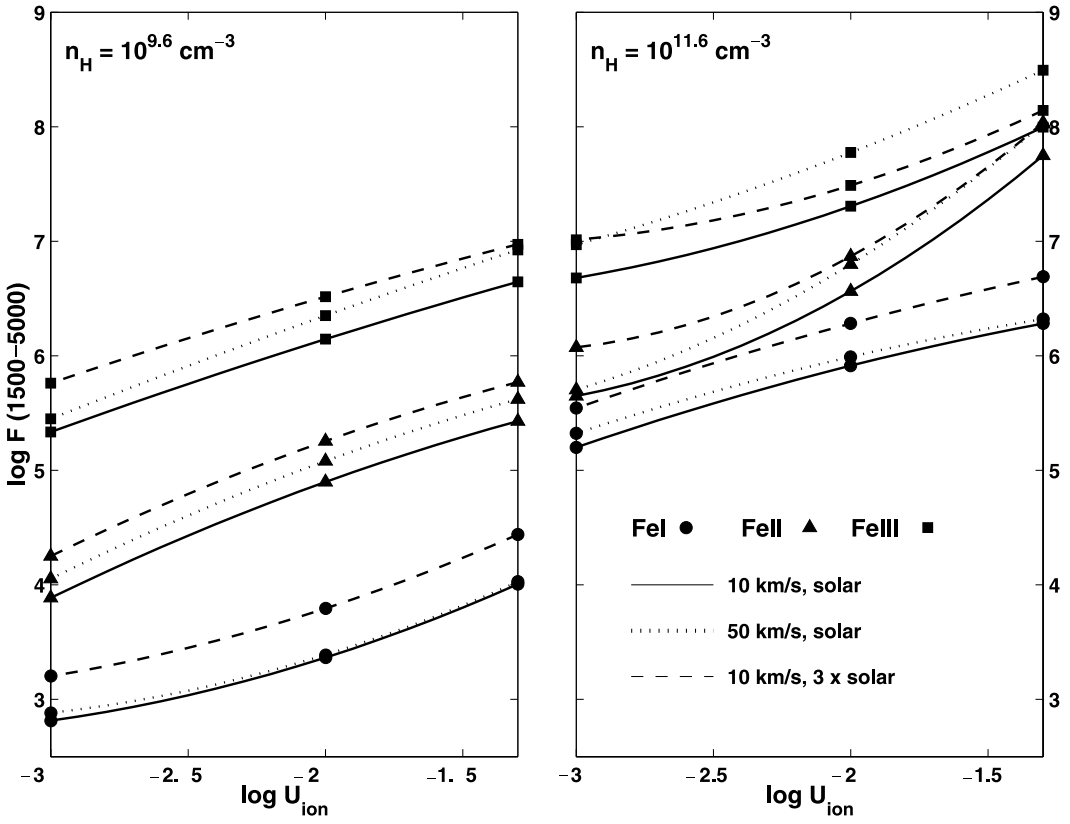

FIG. 6.—Dependence of the Fe I, Fe II, and Fe III line fluxes, in ergs cm^{-2} s^{-1}, summed over the wavelength interval 1500–5000 Å, on the single-zone BLR cloud parameters of Table 2. The effect of tripling the iron abundance and of increasing the cloud turbulent velocity from 10 to 50 km s^{-1} is also shown. The symbols identify the iron ions as in the right-hand panel.

with a solar iron abundance and minimal turbulent velocity (10 km s^{-1}) with the I Zw 1 template. In these comparisons, the calculations have been broadened by convolution with a Gaussian to 900 km s^{-1} FWHM (Vestergaard & Wilkes 2001), and the template has been normalized to the median model flux in the region of strongest Fe III flux included in the template wavelength region, 1800–2000 Å.

In discussing this comparison, it should be emphasized again that all our calculations are for a single BLR cloud with a single ionization parameter and total particle density. The predicted spectrum is then broadened by convolution with a Gaussian to compare to the template. The actual I Zw 1 emitting region is expected to be considerably more complex. It is likely that a range of BLR cloud parameters contribute to the observed Fe flux (as in the locally optimally emitting cloud model of Baldwin et al. (1995), for example) with the overall spectrum shape determined by the (poorly understood) geometry and velocity field within the BLR.

A further possible caveat to keep in mind when viewing a simple, direct comparison to the I Zw 1 spectrum comes from Véron-Cetty et al. (2004). They have constructed an optical Fe II template (3535–7530 Å) for I Zw 1 using a simultaneous fit of four velocity systems: a broad, Lorentzian system, and three narrow-line, Gaussian systems. Based on this multicomponent fit, they argue that the spectrum of I Zw 1 is unusual in that there is a low-excitation, narrow-line system that emits both forbidden and permitted Fe II transitions. In proposing their BLR template, Véron-Cetty et al. remove the narrow-line permitted Fe II component, which leads to significant differences with earlier templates, such as that of Boroson & Green (1992). The Vestergaard & Wilkes template has not been constructed in this fashion. While using multicomponent fits to remove non-Fe features, and to help separate the Fe II–Fe III emission, Vestergaard & Wilkes caution *against* identifying any of the individual fit components with a physical emitting region.

Among the models considered in Figure 7, the higher density, intermediate ionization parameter model u20h11 does a good job of reproducing the overall level of the Fe II UV emission line strength in the 2000–2500 Å region given the normalization to the Fe III flux between 1800–2000 Å. Thus, we find that there is, in principle, no problem in accounting for the relative amount of UV Fe II–Fe III flux from I Zw 1, even with a crude, single-zone model. While inspection of Figure 7 clearly reveals a strong correlation between the model and the empirical template, there are several disagreements in detail. In the principle Fe III wavelength region, 1800–2000 Å, the relative strengths of individual features are not correctly reproduced. Most notable, however, is the failure of the basic model to correctly reproduce the strength of the Fe III feature near 2418 Å identified by Laor et al. (1997). This strong feature is associated with Fe III multiplet UV47, the intersystem transition $z\ ^7P^o–a\ ^5S^e$, giving (identified) features near 2418.58 Å ($J = 3–2$, $f_{ij} = 0.0027$) and 2438.18 Å ($J = 2–2$, $f_{ij} = 0.0011$). Finally, some of the disagreement in the 2200–2600 Å region can be traced to our use of a limited Fe II model atom.[6]

[6] See Table 3 of SP03. Transitions with lower energies well above ~6 eV, or involving levels from the doublet spin system, are not included in the current work.

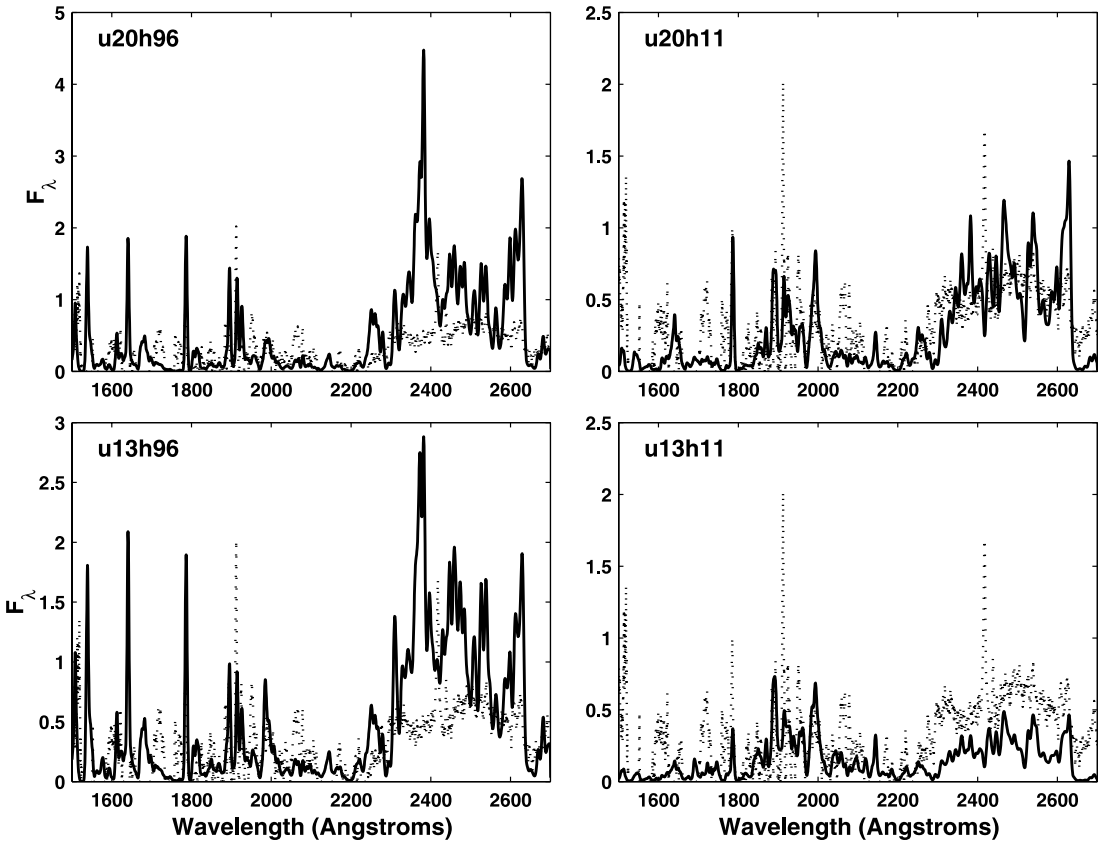

FIG. 7.—Comparison of the far-UV Fe II–Fe III flux (*thick black line*) predicted by four BLR models of Table 2 with the empirical UV Fe II–Fe III template of Vestergaard & Wilkes (2001, *thin dotted line*). All models assumed a turbulent velocity of 10 km s^{-1}, the solar iron abundance, and were broadened by convolution with a Gaussian of FWHM = 900 km s^{-1}. The flux, F_λ, is in units of 10^{-14} ergs cm^{-2} s^{-1} $Å^{-1}$, and the calculations have been normalized to the mean template flux between 1800 and 2000 Å.

To assess the seriousness of these discrepancies, we have performed additional calculations along two fronts: first, we considered predictions of models in which the highly uncertain Fe-H charge-exchange reactions were omitted. As noted in § 4, omission of these rates can substantially alter the iron ionization balance for certain models; second, we have performed a series of Monte Carlo simulations to assess the effect errors in the basic atomic data have on the predicted Fe III line fluxes. We shall first discuss models omitting charge-exchange reactions.

8.1. *Charge-Exchange and* Fe III *UV47 in I Zw 1*

The important role played by the rather uncertain Fe-H charge exchange reaction rates motivated us to compute a series of models in which these rates were omitted. The predicted iron ionization balances have already been discussed in § 4, with the results shown in Figure 3. The predicted flux of model u20h96 without charge-exchange reactions is shown in Figure 8, and these predictions may be compared with Figures 4 and 7. As expected by the change in the ionization balance shown in Figure 3, the model without charge-exchange reactions has a lower Fe II flux and a higher Fe III flux. In fact, normalizing the predicted Fe III fluxes to the observed template in the interval 1800–2000 Å now results in a much better level of predicted UV Fe II flux as compared to Figure 7. In addition, conspicuous in the model omitting charge-exchange reactions is the presence of strong lines of Fe III multiplet UV47. However, while there is now a strong predicted feature at 2418 Å corresponding to Fe III, the fit to the Fe II flux contains strong features for $\lambda \leq 2400$ Å, centered around Fe II 2382.04 Å ($z\ ^6F^o$–$a\ ^6D^e$), which have no counterpart (in terms of observed strength) in the empirical template.

We have also explored the possibility that the Fe III 2400 Å feature is further strengthened by numerous, blended Fe II transitions by merging our predicted Fe III fluxes with the more extensive Fe II fluxes of SP03 based on an 829 level Fe II model atom. However, such merged line lists did not help to improve the fit by much.

In addition, we have found that the higher density models ($\log n_H = 11.6$), including the best-fit model to the overall UV Fe II–Fe III flux of Figure 7, u20h11, are little affected by the neglect of Fe-H charge-exchange reactions and do not predict strong Fe III UV 47 features.

8.2. *Monte Carlo Simulation Estimates for Error Bounds*

Given that all of the models presented have some shortcomings when compared to the Vestergaard & Wilkes template, it is important to assess the accuracy to which the iron line fluxes can be computed. This is a complex question, encompassing everything from the accuracy of the underlying BLR cloud model(s) and the approximations used in the numerical methods to the accuracy of the underlying atomic data. In this work, we will address only the latter issue by asking how accurately the iron line fluxes can be predicted given the sometimes large uncertainties in the basic atomic data. Even this question is not completely straightforward. For

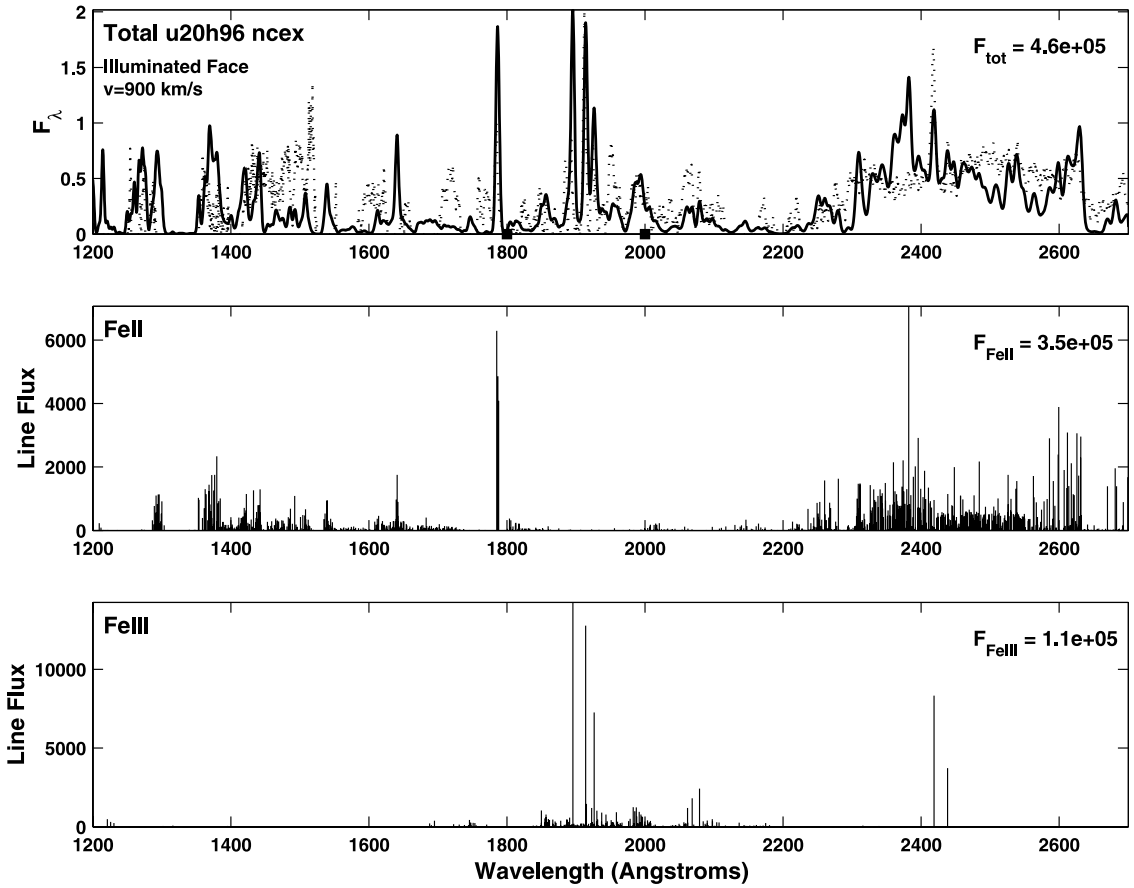

FIG. 8.—Top panel compares the far-UV Fe II–Fe III flux (*thick black line*) predicted by model u20h96 without Fe-H charge-exchange reactions with the empirical template of Vestergaard & Wilkes (2001, *dotted line*). In the top panel, the flux, F_λ, is in units of 10^{-14} ergs cm^{-2} s^{-1} Å^{-1}. The two lower panels show the contributions of the individual iron ions in terms of the predicted line fluxes (in units of ergs cm^{-2} s^{-1}).

example, a single A_{ji}-value clearly affects the flux in the $j \rightarrow i$ radiative transition. However, through the coupling of the atomic level populations by the statistical equilibrium equations, and the global coupling of the emitting volume through the transfer of radiation, a single A_{ji}-value can possibly affect the fluxes in many lines. And similar observations can be made, in principle, for all of the remaining atomic data, including the photoionization and recombination rates and the collisional excitation and de-excitation rates. To address all of these interconnections in a consistent manner, we have turned to the Monte Carlo simulation technique used by Sigut (1996). Each fundamental atomic parameter (A_{ji}-value, effective collision strength, photoionization cross section, collisional ionization cross section, and charge-transfer reaction rate) is assigned an uncertainty. Given these uncertainties, a set of atomic data is randomly realized and used to solve the radiative transfer-statistical equilibrium problem for the iron fluxes. Then, a new set of atomic data is randomly realized and the predicted fluxes for these new data found. This sequence is repeated, and the width of the distribution of each line flux can be taken as a measure of its uncertainly.

Table 4 lists the basic atomic data uncertainties adopted for our collection of iron atomic data. The error assignment is kept deliberately simple; in principle, uncertainties could be assigned on a transition by transition basis. The ***R***-matrix collision strengths (cbb rates) for low ionization states computed under the Iron Project are the most accurate ones available. However, they also display extremely complicated structure due to autoionizing resonances in the near-threshold region, which dominates the rate coefficient at $T \sim 10^4$ K. Therefore, uncertainties as large as a factor of 2–3 for individual transitions can not be ruled out. The A_{ji}-values (rbb rates) are expected to be more accurate; however, significant errors may still be present, particularly in several calculations where relativistic effects have not been considered in an ab initio manner. Such calculations are now in progress, but the computations are about an order of magnitude more difficult that those in LS coupling (see Nahar 2003).

The distribution of the random scalings is also kept very simple: a set of uniform random deviates, r, is computed with

TABLE 4

UNCERTAINTIES ASSIGNED TO THE IRON ATOMIC DATA

Type	Atomic Parameter	Uncertainty[a]	Notes
rbb	A_{ji}	1.50	***R***-matrix
rbb	A_{ji}	2.00	Semiempirical
rbf[b]	$\sigma_{i\kappa}(\nu)$	1.50	***R***-matrix
cbb	$\gamma_{ij}(T_e)$	1.25	***R***-matrix
cbb	$\gamma_{ij}(T_e)$	10.0	Gaunt factor approx.
cbf	$\Upsilon_{i\kappa}(T_e)$	10.0	Seaton approx.
cex	$r_{i\kappa}(T_e)$	10.0	Landau-Zener approx.

[a] The uncertainty is denoted p in the text.

[b] The recombination rate to each individual level is related to the photoionization cross section (rbf) through the Einstein-Milne relation.

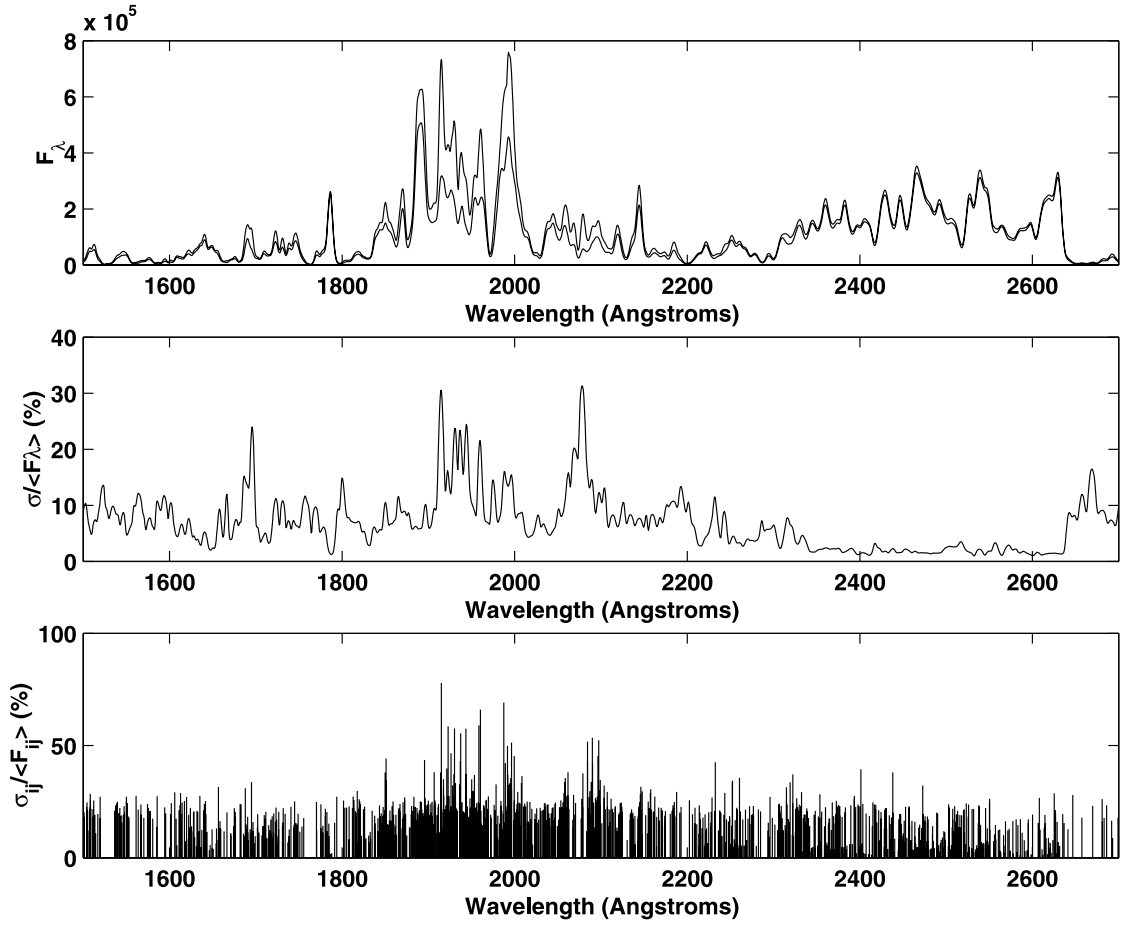

FIG. 9.—Predicted UV Fe II–Fe III flux from 26 randomly realized atomic models (see Table 4) for BLR model u13h11 (Table 2). The top panel shows the minimum and maximum flux (in ergs cm^{-2} s^{-1} $Å^{-1}$) predicted at each wavelength, and the middle panel shows the standard deviation of the predicted flux at each wavelength expressed as a percentage of the average flux at that wavelength. The spectrum was broadened with a Gaussian of FWHM of 900 km s^{-1}. The bottom panel shows the predicted uncertainty in the individual line fluxes, F_{ij} (in units of ergs cm^{-2} s^{-1}), for the 2300 strongest Fe II–III lines in the model.

the RAN2 algorithm of Press et al. (1992). Given the uncertainty assignment, p, from Table 4, a uniform set of deviates for the logarithm of the scaling is found from the linear relation $l = a + r(b - a)$, where $a = -\log_{10}(p)$ and $b = \log_{10}(p)$. The actual set of scalings, d, is taken as $d = 10^l$. This procedure ensures the following common-sense property of the scalings: for example, if a charge-exchange rate is assumed accurate to within a factor of 100, then one might expect the a scaling from 0.1 to 1.0 to be as likely as one from 1 to 10. However, this procedure also results in the mean scaling being different from 1, namely $\bar{d} = (p - p^{-1})/[\ln 10(b - a)]$; for example, the mean scaling for $p = 100$ is about 10.8. Thus, the most probable value for the rate is not that adopted in the default (unscaled) atomic model. However, given the uncertainty (a factor of 100 in this case), we do not consider this deviation significant.

Figure 9 summarizes the uncertainties due to the atomic data uncertainties in Table 4 on the predicted Fe II–Fe III flux for model u13h11. Although not the best fit to the Vestergaard & Wilkes template, it is representative of the models considered in this work. Fe-H charge-exchange reactions were included in this calculation, although assumed uncertain to within a factor of 10 (Table 4). The top panel displays the minimum and maximum predicted flux at each wavelength, and the middle panel shows the standard deviation of each predicted flux expressed as a percentage of the average flux at that wavelength. The largest uncertainties approach 30% for the Fe III features near 2000 Å. This reflects mostly the scaling of the charge-exchange reaction rates, which strongly affects the Fe II–Fe III ionization balance. Much smaller uncertainties are predicted for the bulk of the Fe II emission; these smaller uncertainties reflect, to some extent, the large number of individual Fe II transitions contributing to each wavelength in the broadened spectrum (see Fig. 9, *bottom*), each with an individually scaled uncertainty following Table 4. In interpreting this figure, it should be kept in mind that, at best, it presents minimum theoretical uncertainties given that only errors in the basic atomic data are included. Nevertheless, significant uncertainty in the predicted Fe III line flux in the vicinity of 1900 Å is seen, and this might help to explain some of the detailed discrepancies with the I Zw 1 template in this region seen in Figure 7.

9. DISCUSSION

The primary aim of this continuing project is to incorporate advanced methods of non-LTE radiative transfer from stellar astrophysics into emission line analysis of AGNs. In the current work, we have provided predictions for the entire low-ionization spectrum of iron, focusing on Fe III. Given the preliminary nature of the models, and the use of only single-zone BLR cloud models, a reasonable fit to the Fe II–Fe III UV template of Vestergaard & Wilkes for I Zw 1 was obtained. We are currently exploring multicloud BLR models along the

lines of the locally optimally emitting cloud models of Baldwin et al. (1995) to see if an improved fit to the I Zw 1 UV template can be obtained. We also intend to compare the predictions of such a model to the new optical I Zw 1 template of Véron-Cetty et al. (2004).

An aspect in which our treatment is incomplete is in the detailed treatment of the Fe IV atom, the dominant ionization state in the fully ionized, optically thin region of BLR models. The atomic data for Fe IV are in hand, computed from the Iron Project, and we plan to incorporate them into a further extension of the present work on par with Fe II and Fe III. The Fe IV lines may also contribute to UV spectra of BLR; for example, see observations of the Orion nebula using the *Hubble Space Telescope* (Rubin et al. 1997).

In addition, the 2418 Å feature in the computed and observed Fe III spectra offers a diagnostic of atomic processes and physical conditions and of uncertainties in atomic data. The combined role of these factors in determining the intensity of this emission feature may be illustrated by considering level-specific $e^- + \mathrm{Fe}^{3+} \rightarrow \mathrm{Fe}^{2+}$ recombination. An increase in the recombination-cascade rates might lead to (1) less of a role for charge-exchange, as inferred by the non–charge-exchange models, (2) enhancement of the 2418 Å feature due to recombination contribution to the Fe III line, and (3) less flux in Fe II shortward of 2400 Å, consistent with observations. The present recombination rates were derived from level-specific photoionization cross sections of Fe III computed in LS coupling (Nahar & Pradhan 1994). Later work has shown (Pradhan et al. 2001; Nahar & Pradhan 2003) that near-threshold resonance complexes may affect the recombination rates by up to several factors. It is necessary to consider relativistic fine structure and resolve the resonance complexes in great detail (excited metastable state cross sections are affected much more than the ground state). Nahar & Pradhan (2003) have developed a unified scheme for calculations of electron-ion recombination, including both the radiative and the dielectronic recombination processes. Such level-specific calculations for total recombination into the Fe III levels may possibly resolve the discrepancy in the observed and computed intensities of the 2418 Å feature.

It is therefore not an exaggeration to say that in spite of the present scale of this effort, both in terms of atomic physics and radiative transfer, considerable work is still needed to improve the models.

We would like to thank Marianne Vestergaard for providing the UV I Zw 1 iron template. This work was supported by the Natural Sciences and Engineering Research Council of Canada (T. A. A. S.) and by the US National Science Foundation and NASA (A. K. P. & S. N.).

REFERENCES

Arav, N., Barlow, T. A., Laor, A., & Blandford, R. D. 1997, MNRAS, 288, 1015
Baldwin, J. A., Ferland, G., Korista, K., & Verner, D. 1995, ApJ, 455, L119
Baldwin, J. A., et al. 1996, ApJ, 461, 664
Bautista, M. A., & Pradhan, A. K. 1997, A&AS, 122, 167 (IP.XX)
Bergeron, J., & Knuth, D. 1980, A&A, 85, L11
Boroson, T. A., & Green, R. F. 1992, ApJS, 80, 109
Carlsson, M., Rutten, R. J., & Shchukina, N. G. 1992, A&A, 253, 567
Collin-Souffrin, S., Joly, M., Pequignot, D., & Dumont, S. 1986, A&A, 166, 27
Collin-Souffrin, S., Hameury, J.-M., & Joly, M. 1988, A&A, 205, 19
Dumont, A. M., & Collin-Souffrin, S. 1990, A&A, 229, 313
Ekberg, J. O. 1993, A&AS, 101, 1
Elitzur, M., & Netzer, H. 1985, ApJ, 291, 464
Ferland, G. J. 1991, HAZY: An Introduction to CLOUDY, OSU Int. Rep. 91-01
Flower, D. 1990, Molecular Collisions in the Interstellar Medium (Cambridge: Cambridge Univ. Press)
Graham, M. J., Clowes, R. G., & Campusano, L. E. 1996, MNRAS, 279, 1349
Hummer, D. G., Berrington, K. A., Eissner, W., Pradhan, A. K., Saraph, H. E., & Tully, J. A. 1993, A&A, 279, 298 (IP.I)
Joly, M. 1993, Ann. Phys. Fr., 18, 241
Kingdon, J. B., & Ferland, G. J. 1996, ApJS, 106, 205
Kurucz, R. L., & Bell, B. 1995, Atomic Line Data, Kurucz CD-ROM No. 23 (Cambridge: SAO)
Kwan, J. K., Cheng, F., Fang, L., Zheng, W., & Ge, J. 1995, ApJ, 440, 628
Kwan, J. K., Krolik, J. H. 1981, ApJ, 250, 478
Laor, A., Jannuzi, B. T., Green, R. F., & Boroson, T. A. 1997, ApJ, 489, 656
Mathews, W. G., & Ferland, G. J. 1987, ApJ, 323, 456
Nahar, S. N. 1995, A&A, 293, 967 (IP.VII)
———. 2003, in ASP Conf. Ser. 288, Stellar Atmosphere Modeling, ed. I. Hubeny, D. Mihalas, & K. Werner (San Francisco: ASP), 651
Nahar, S. N., & Pradhan, A. K. 1994, J. Phys. B, 27, 429
———. 1996, A&AS, 119, 507 (IP.XVII)
———. 2004, in Radiation Processes In Physics and Chemistry ed. R. H. Pratt & S. T. Manson (North Holland: Elsevier), 323
Netzer, H. 1980, ApJ, 236, 406
———. 1990, Saas-Fee Advanced Course 20, Active Galactic Nuclei, ed. T. J.-L. Courvoisier & M. Mayor (Heidelberg: Springer), 57
Netzer, H., & Wills, B. J. 1983, ApJ, 275, 445
Neufeld, D. A., & Dalgarno, A. 1987, Phys. Rev. A, 35, 3142
Osterbrock, D. E. 1989, Astrophysics of Gaseous Nebula and Active Galactic Nuclei (Mill Valley: University Science Books)
Pelan, J., & Berrington, K. A. 1997, A&AS, 122, 177 (IP.XXI)
Penston, M. V. 1987, MNRAS, 229, 1P
Peterson, B. M., Pogge, R. W., & Wanders, I. 1999, in ASP Conf. Ser. 175, Structure and Kinematics of Quasar Broad-Line Regions, ed. C. M. Gaskell, W. N. Brandt, M. Dietrichm, D. Dultzin-Hacyan, & M. Eracleous (San Francisco: ASP), 41
Pradhan, A. K. Nahar, S. N., & Zhang, H. L. 2001, ApJ, 549, L265
Press, W. H., Teukolsky, S. A., Vetterling, W. T., & Flannery, B. P. 1992, Numerical Recipes (Cambridge: Cambridge Univ. Press)
Rodríguez-Ardila, A., Viegas, S. M., Pastoriza, M. G., & Prato, L. 2002, ApJ, 565, 140
Rubin, R. H., et al. 1997, ApJ, 474, L131
Rudy, R. J., Lynch, D. K., Mazuk, S., Venturini, C. C., Puetter, C., & Hamann, F. 2001, PASP, 113, 916
Rudy, R. J., Mazuk, S., Puetter, C., & Hamann, F. 2000, ApJ, 539, 166
Sigut, T. A. A. 1996, ApJ, 473, 452
Sigut, T. A. A., & Lester, J. B. 1996, ApJ, 461, 972
Sigut, T. A. A., & Pradhan, A. K. 1998, ApJ, 499, L139
———. 2003, ApJS, 145, 15 (SP03)
Van Regemorter, H. 1962, ApJ, 136, 906
Véron-Cetty, M.-P., Joly, M., & Véron, P. 2004, A&A, 417, 515
Verner, E. M., Verner, D. A., Korista, K. T., Ferguson, J. W., Hamann, F., & Ferland, G. J. 1999, ApJS, 120, 101
Vestergaard, M., & Wilkes, B. J. 2001, ApJS, 134, 1
Wills, B. J., Netzer, H., Uomoto, A. K., & Wills, D. 1980a, ApJ, 237, 319
Wills, B. J., Netzer, H., & Wills, D. 1980b, ApJ, 241, L1
———. 1985, ApJ, 288, 94
Zhang, H. L. 1996, A&AS, 199, 523 (IP.VXIII)
Zhang, H. L., & Pradhan, A. K. 1995, A&A, 293, 953 (IP.VI)